New Reaction Pathway Induced by Plasmon for Selective Benzyl Alcohol Oxidation on BiOCl Possessing Oxygen Vacancies

Hao Li,[†,‡] Feng Qin,[†] Zhiping Yang,[‡] Ximin Cui,[†] Jianfang Wang,[*,†] and Lizhi Zhang[*,‡]

[†]Department of Physics, The Chinese University of Hong Kong, Shatin, Hong Kong SAR, China

[‡]Key Laboratory of Pesticide and Chemical Biology of Ministry of Education, Institute of Environmental Chemistry, College of Chemistry, Central China Normal University, Wuhan 430079, China

S *Supporting Information*

ABSTRACT: Selective organic transformation under mild conditions constitutes a challenge in green chemistry, especially for alcohol oxidation, which typically requires environmentally unfriendly oxidants. Here, we report a new plasmonic catalyst of Au supported on BiOCl containing oxygen vacancies. It photocatalyzes selective benzyl alcohol oxidation with O_2 under visible light through synergistic action of plasmonic hot electrons and holes. Oxygen vacancies on BiOCl facilitate the trapping and transfer of plasmonic hot electrons to adsorbed O_2, producing $\bullet O_2^-$ radicals, while plasmonic hot holes remaining on the Au surface mildly oxidize benzyl alcohol to corresponding carbon-centered radicals. The hypothesized concerted ring addition between these two radical species on the BiOCl surface highly favors the production of

benzaldehyde along with an unexpected oxygen atom transfer from O_2 to the product. The results and understanding acquired in this study, based on the full utilization of hot charge carriers in a plasmonic metal deposited on a rationally designed support, will contribute to the development of more active and/or selective plasmonic catalysts for a wide variety of organic transformations.
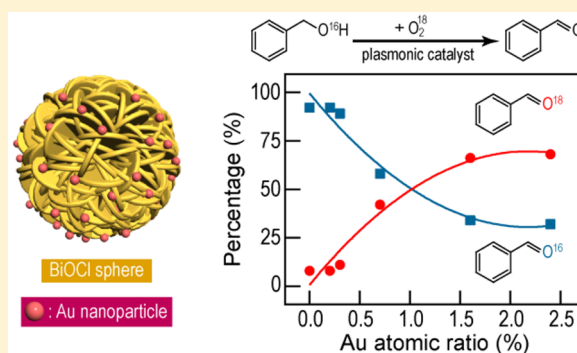
INTRODUCTION

Selective oxidation of alcohols is a fundamental organic transformation of great industrial and laboratorial importance, because the corresponding carbonyl compounds, aldehydes or ketones, serve as versatile building blocks for the synthesis of pharmaceuticals and fine chemicals. However, traditional noncatalytic methods for the oxidation of alcohols feature a severe drawback that the oxidants, such as permanganate and dichromate, are commonly environmentally unfriendly. Tremendous efforts have therefore been devoted to the design of catalytic systems that use O_2 as the primary oxidant, which is clean and abundant, producing H_2O or H_2O_2 as the sole byproduct.[1,2] While many successful examples have been demonstrated over noble metals or transition metal complexes under alkaline conditions, the recent use of solar energy and O_2 to drive this reaction by semiconductor photocatalysts provides a more sustainable pathway.[3−7] Unfortunately, photocatalytic aerobic alcohol oxidation has still typically suffered from low efficiency and poor selectivity.[8−10] The weak interaction of O_2 with the surfaces of photocatalysts, especially with defect-free surfaces, is a critical issue for the inefficiency of photocatalytic alcohol oxidation, because the participation of O_2, either directly as a reactant or indirectly as an electron acceptor, should be accompanied by interfacial electron transfer.[5,8,11,12] Another critical issue for the poor selectivity is the strong oxidizing power of photogenerated holes, which can cause an unavoidable nonselective process to overoxidize or mineralize

alcohols.[10,13,14] Therefore, the challenge for achieving selective alcohol oxidation is to develop photocatalysts that can strongly interact with O_2 but do not generate any strongly oxidative holes.

Similar to semiconductor photocatalysts, noble metals, such as Au and Ag, have recently proven to be an efficient agent for harvesting solar energy for chemical processes due to localized surface plasmon resonance (LSPR). LSPR refers to the collective oscillation of conduction-band (CB) electrons that are in resonance with the oscillating electric field of incident light. The decay of excited LSPR can generate hot electrons and holes to initiate chemical reactions.[15−17] Of particular interest is the oxidizing ability of hot holes within Au, which is thought to be much milder than that of holes in the valence band (VB) of most photocatalytic semiconductors, offering a possibility for the application in oxidative organic transformations.[18−20] However, hot carriers suffer from rapid decay. Therefore, an inorganic support is often integrated with Au to promote their separation.[21−23] Because the surface properties of the support are pivotal in determining both the dynamics of plasmonic hot carriers and the interaction with reactants, we reason that a novel catalyst can be designed for selective alcohol oxidation if the support is well functionalized.

Here, we report a new plasmonic catalyst that is made of Au nanoparticles (NPs) deposited on BiOCl possessing oxygen vacancies (OVs). The introduction of OVs enables interesting synergistic action of plasmonic hot electrons and holes for selective alcohol oxidation, leading to a new reaction pathway, where the oxygen atom in up to 66% of the product molecule is from O_2 instead of the alcohol reactant molecule. Mechanistic insights into the high selectivity as well as the synergistic effect are proposed and discussed on the basis of experimental results.

■ EXPERIMENTAL SECTION

Catalyst Preparation. To prepare BiOCl with OVs, $Bi(NO_3)_3 \cdot 5H_2O$ (3 mmol) was added slowly into ethylene glycol solution (16 mL) containing a stoichiometric amount of KCl. The mixture was then poured into a 20 mL Teflon-lined stainless autoclave and reacted at 160 °C for 12 h under the autogenous pressure. The resultant precipitate was collected and washed consecutively with deionized water and ethanol to remove residual ions. The final product was dried at 80 °C in air. Defect-free BiOCl was prepared by calcining BiOCl-OV in O_2 atmosphere at 300 °C in a tube furnace (OTF-1200X, MTI Corporation) for 4 h. For the microwave synthesis of Au NPs on the supports, BiOCl or BiOCl-OV (0.1 g) was dispersed in ethylene glycol (30 mL). $HAuCl_4$ in a calculated amount was added into the mixture. The resultant solution was placed in a microwave reactor system (MAS-1, Shanghai Xinyi), and irradiated under microwave at 160 °C for 12 min. The obtained hybrid materials are denoted as Au-BiOCl and Au-BiOCl-OV. By changing the amount of bismuth precursor during the synthesis to 0.5, 1, or 2 mmol, BiOCl with lower concentrations of OVs can be prepared. The colloidal Au nanosphere sample with diameters in the range of 30−35 nm was purchased from NanoSeedz.

For the preparation of fluorinated Au-BiOCl-OV, typically, 50 mg of the as-prepared Au-BiOCl-OV was dispersed in 10 mL of NaF (0.01 mol L^{-1}) through ultrasonication for 1 h. The fluorinated product was collected by centrifugation, and then dried at 80 °C.

For the adsorption of H_2O_2 on Au-BiOCl-OV, Au-BiOCl-OV (20 mg) was added into double-distilled water (2 mL) containing H_2O_2 (0.1 mmol). The obtained mixture was continuously stirred in dark for 2 h to ensure the full adsorption of H_2O_2 on the surface of Au-BiOCl-OV. The mixture solution was subsequently centrifuged. The resultant precipitate was collected without any washing and dried in a vacuum oven at 15 °C before further characterization.

Photocatalytic Benzyl Alcohol Oxidation. Typically, the photocatalyst (50 mg) was suspended in acetonitrile (10 mL) containing benzyl alcohol (BO) (0.5 mmol) in a 20 mL round-bottomed flask. After the solution was bubbled with O_2 for 30 min, the flask was sealed with a balloon that was prefilled with O_2 at a pressure of ~1 atm. Subsequently, the solution was magnetically stirred for 1 h in dark to ensure the establishment of equilibrium between adsorption and desorption. The temperature was maintained around 25 °C by use of a water bath. After irradiation under a 300 W Xe lamp with a 420 nm cutoff filter (PLS-SEX300C, Beijing Perfectlight Technology) or a 10 W ultraviolet (UV) light source for certain time, 2 mL of the suspension was collected, centrifuged, and filtered through a 0.22 mm nylon syringe filter. The concentration of BO was measured using a high-performance liquid chromatography (Shimadzu LC-20A, Japan, TC-C18 reverse phase column). The conversion percentage of BO and the selectivity for benzaldehyde (BD) are defined as conversion (%) = $[(C_0 - C_{BO})/C_0] \times 100\%$ and selectivity (%) = $[C_{BD}/(C_0 - C_{BO})] \times 100\%$, where C_0 is the initial concentration of BO, C_{BO} and C_{BD} are the concentrations of the detected BO and BD, respectively. $^{18}O_2$-labeling experiments were conducted under similar conditions to the photocatalytic oxidation of BO except that the normal O_2 atmosphere was replaced by $^{18}O_2$. Identification of the oxidation product of BD was conducted on gas chromatography mass spectrometry (GC-MS, Agilent Technologies, GC6890N, MS 5973) that was equipped with a HP-5MS capillary column (30 m × 0.25 mm,

0.25 μm). According to the NIST mass spectral database, the product was deduced from the MS/MS mode and analyzed by the scan mode.

Electrochemical Measurements. To prepare the electrodes, the catalyst was dispersed in chitosan solution (0.5 wt %) to form a 10 mg mL^{-1} solution. 0.3 mL of the resultant solution was then dip-coated on the pretreated indium tin oxide (ITO) or fluorine-doped tin oxide (FTO) surface and allowed for drying in a vacuum oven for 24 h at room temperature. The photocurrent measurements were conducted on an electrochemical workstation (CHI660D Instruments) in a standard three-electrode system with the catalyst as the working electrode, a Pt foil as the counter electrode, a saturated calomel electrode as the reference electrode, and an aqueous Na_2SO_4 solution (0.5 mol L^{-1}) as the electrolyte. Before measurements, Ar gas was purged into the Na_2SO_4 solution for 30 min to remove dissolved O_2. The electrolyte was kept under purging during the photocurrent measurements. The 300-W xenon lamp with a 420 nm cutoff filter or a light-emitting diode (LED) lamp (UVEC-4II, 4.5 W, Shenzhen Lamplic Technology, China) was utilized as the light source for the photocurrent measurements. The Mott−Schottky experiments were conducted to evaluate the band positions of the as-prepared samples in the potential range from −0.5 to +0.2 V at a potential step of 0.05 V and a frequency of 997 Hz.

Detection of Reactive Species. Nitroblue tetrazolium (5×10^{-5} M, exhibiting an absorption maximum at 259 nm) was used to determine the amount of $\bullet O_2^-$ generated by the catalyst. The production of $\bullet O_2^-$ in the suspension was quantitatively analyzed by measuring the concentration of nitroblue tetrazolium on a UV/visible spectrophotometer. The concentration of H_2O_2 was determined by a fluorescence method through the use of a fluorometer with the excitation and emission wavelengths set at 315 and 409 nm, respectively. The fluorescence reagent was prepared by adding 2.7 mg of p-hydroxyl phenyl acetic acid and 1 mg of horseradish peroxidase in 10 mL of potassium hydrogen phthalate buffer solution (8.2 g L^{-1}). This reagent should be stored below 4 °C. Typically, 50 mg of the catalyst was added to 100 mL of deionized water under stirring. At different time intervals under the visible light irradiation of the Xe lamp, 2 mL of the suspension was collected and filtered through a 0.22 mm nylon syringe filter. Then, 50 mL of the fluorescence reagent was added to the filtered suspension. After 10 min of reaction, 1 mL of NaOH solution (0.1 M) was added before the subsequent fluorescence measurements. $\bullet O_2^-$ and carbon-centered radicals were detected with electron paramagnetic resonance (EPR) spectroscopy. 5,5-Dimethyl-1-pyrroline-N-oxide (DMPO) was used to in situ trap the spin-reactive species. All of the spin trapping EPR measurements for the detection of the spin adducts were carried out by use of the settings of 10 mW microwave power, 100-G scan range, and 1-G modulation. The active trapping experiments were conducted by adding different types of excess scavengers (10 mM) into BO before the photocatalytic reaction. $AgNO_3$ was employed for the trapping of electrons, benzoquinone for $\bullet O_2^-$, sodium sulfide for holes, and butylated hydroxytoluene for carbon-centered radicals.

Characterization. X-ray diffraction (XRD) patterns were recorded on a Rigaku D/MAX-RB diffractometer with monochromatized Cu Kα radiation (λ = 0.15418 nm). Scanning electron microscopy (SEM) images were acquired on an FEI Quantum 400F microscope operated at 20 kV. High-resolution transmission electron microscopy (HRTEM) imaging, high-angle annular dark-field scanning transmission electron microscopy (HAADF-STEM) characterization, and energy-dispersive X-ray (EDX) elemental mapping were carried out on an FEI Tecnai F20 microscope operated at 200 kV. Absorbance spectra were measured using a UV/visible spectrophotometer (UV-2550, Shimadzu, Japan). Fluorescence measurements were performed on a FluoroMax-P fluorometer. Extinction spectra were taken on a Hitachi U-3501 UV/visible/near-infrared spectrophotometer with 1.0 cm quartz cuvettes. Low-temperature EPR spectra were acquired on a Bruker EMX EPR spectrometer (Billerica, MA). X-ray photoelectron spectroscopy (XPS) measurements were performed on a PerkinElmer PHI 5000C system. All binding energies were calibrated by use of contaminant carbon (C 1s at 284.6 eV) as a reference. The system for steady-state and transient surface photovoltage (SPV) measurements
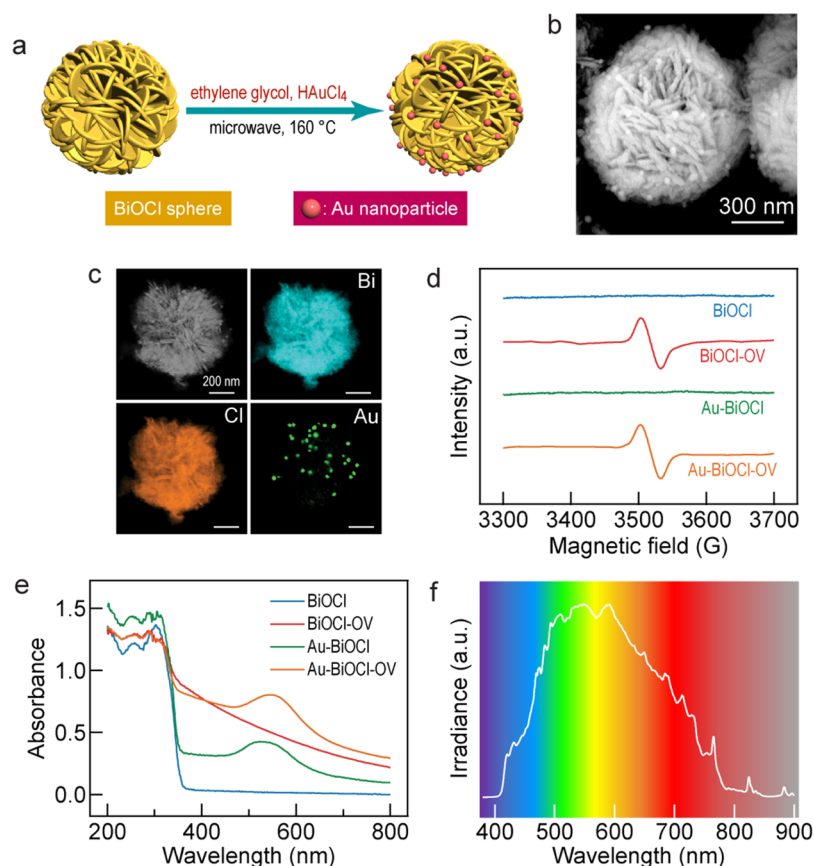
Figure 1. Characterization of the photocatalysts. (a) Schematic illustration of the synthetic process. (b) Backscattering SEM image of Au-BiOCl-OV. (c) HAADF-STEM image of a single Au-BiOCl-OV microsphere and the corresponding EDX elemental mapping of Bi (turquoise), Cl (orange), and Au (green). The scale bars on the Bi, Cl and Au images are the same as that on the HAADF-STEM image. (d) Low-temperature EPR spectra. (e) Absorption spectra. (f) Irradiance spectrum of the simulated solar light.

included a source of monochromatic light, a lock-in amplifier (SR830-DSP) with a light chopper (SR540), a photovoltaic cell, and a computer. A 500-W xenon lamp (CHFXQ500 W, Global Xenon Lamp Power) in conjunction with a double-prism monochromator (Zolix SBP500) provided monochromatic light as the light source. The samples were examined without further treatment during the SPV measurements, and the contact between the sample and the ITO electrode was nonohmic. Steady-state and time-resolved photoluminescence (PL) measurements were carried out on an FLS900 fluorometer (Edinburgh Instruments). The Au atomic ratios relative to BiOCl were determined by inductively coupled plasma atomic emission spectroscopy (ICP-AES, Shimadzu, ICPS-8100). Fourier transform infrared (FTIR) spectra were recorded on a Nicolet iS50FT-IR spectrometer (Thermo, U.S.A.). The total organic carbon content of the reaction solution was determined by use of a Shimadzu TOC-V CPH analyzer.

Electrodynamic Simulations. The simulations were performed using FDTD solutions 8.7.1 (Lumerical Solutions). During simulations, an electromagnetic pulse in the wavelength range from 400 to 1400 nm was launched into a box containing a target nanostructure. The targeted nanostructure was surrounded by a virtual boundary at an appropriate size. A mesh size of 0.5 nm was employed in calculating the extinction spectra and electric field intensity enhancements of the Au/BiOCl hybrid structure. The refractive index of BiOCl was set to be 2.15. The dielectric function of gold was taken from Johnson and Christy's experimental data.

RESULTS AND DISCUSSION

Catalyst Characterization. Our motivation for employing oxygen-deficient BiOCl as a model support is explained as follows. BiOCl is a typical UV-light-responsive semiconductor.

It has received increasing attention due to its defect-related reactivity. OVs on the surface are the most common type of defects in BiOCl. They provide perfect sites for enhanced O_2 adsorption and activation.[24−26] Moreover, surface OVs with their localized electronic states typically lying below the CB can usually serve as trapping sites for photogenerated electrons to promote the separation of charge carriers as well as charge transfer to adsorbates. All of these merits make oxygen-deficient BiOCl an appropriate support to potentially enhance the utilization efficiency of O_2 as well as the separation efficiency of plasmonic hot carriers from Au without generating strongly oxidative holes under visible light. BiOCl with OVs (BiOCl-OV) was prepared through a simple solvothermal method.[27] SEM imaging revealed that BiOCl-OV is composed of hierarchical microspheres assembled from radically grown nanosheets with their thicknesses around 15 nm (Figure S1a of the Supporting Information). Defect-free BiOCl was prepared by calcining BiOCl-OV under O_2 atmosphere to quench OVs. A rapid microwave-heating method was adopted to deposit Au on the surface of BiOCl or BiOCl-OV to produce Au-BiOCl or Au-BiOCl-OV using ethylene glycol as the reducing agent and $HAuCl_4$ as the Au precursor (Figure 1a). After the microwave reaction, many isolated Au NPs were observed to randomly distribute on the surface of BiOCl-OV (Figure S1b). The Au NPs appear much brighter on the backscattering SEM image due to the heavier atomic mass of Au, allowing for the estimation of the size distribution of the NPs to be in the range of 30−35 nm (Figure 1b and Figure S2).
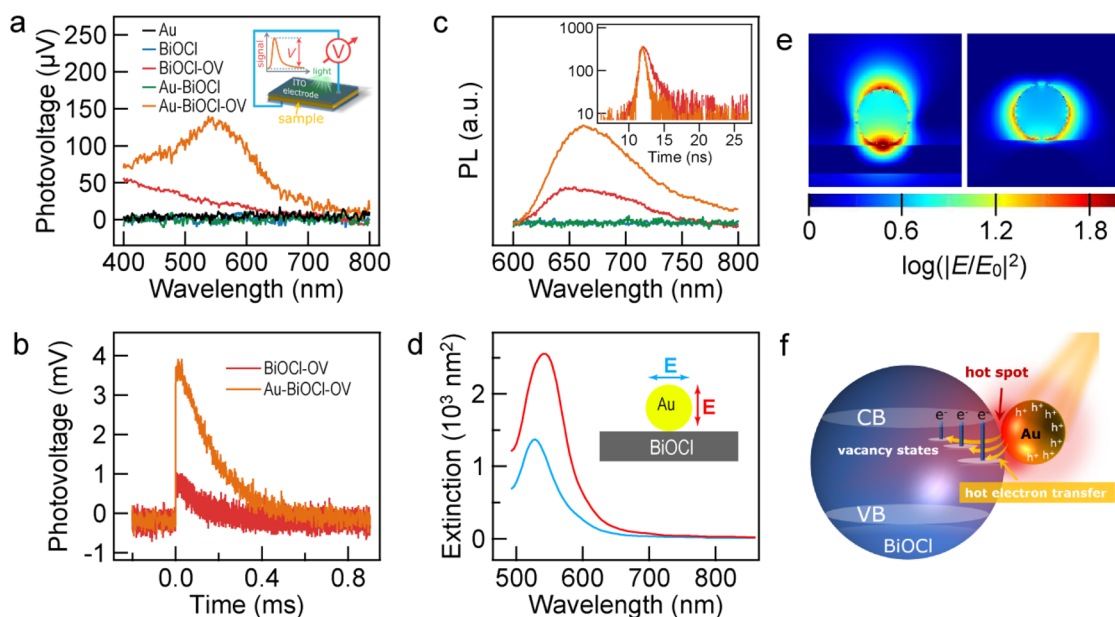
Figure 2. Dynamics of hot carriers. (a) Steady-state SPV spectra of the photocatalysts. The inset shows the schematic of the photovoltaic cell structure, which records the change of the catalyst surface potential signal (V) before and after light irradiation. The SPV measurements were performed with ITO substrates. (b) Transient SPV spectra of the photocatalysts under a 532 nm laser pulse. The decay lifetimes were obtained by fitting against a single-exponential function. (c) Steady-state PL spectra of the photocatalysts. The inset shows the time-resolved PL spectra of BiOCl-OV and Au-BiOCl-OV, which can be fitted using a multiexponential function, $I_{PL}(t) = \sum_{i=1}^{n} A_i e^{t/\tau_i}$, where $I_{PL}(t)$ represents the PL intensity, τ_i is the decay time, and A_i is the amplitude. (d) Simulated extinction spectra of a gold nanosphere of 30 nm in diameter supported on a BiOCl nanosheet of 15 nm in thickness. The schematic in the inset illustrates the out-of-plane (red) and in-plane (blue) polarized excitations relative to the support. (e) Electric field intensity enhancement contours of the Au/BiOCl hybrid system under the out-of-plane (left) and in-plane (right) polarized excitations. The use of such a model is for the purpose of simplicity. (f) Schematic illustration of the hot electron dynamics within Au-BiOCl-OV.

The XRD peak at 38.3° on the tetragonal phase of BiOCl (Figure S1c), which can be indexed to the (111) reflection of metallic Au, and the Au 4f peaks at 83.4 and 87.1 eV detected by XPS (Figure S3a), reveal the metallic nature of the Au NPs. Similar to the case of backscattering SEM imaging, a number of bright Au NPs were seen to be spotted on BiOCl-OV under HAADF-STEM imaging (Figure 1c). Elemental mapping clearly showed the presence of Bi and Cl on the support, and that the bright spots are made of Au (Figure 1c). HRTEM imaging revealed the high crystallinity nature of both BiOCl nanosheets, which have their {001} facets exposed and are the building blocks of the BiOCl microspheres, and Au NPs (Figure S4).

The presence of OVs on BiOCl was first evidenced by low-temperature EPR (Figure 1d). A characteristic OV signal with a g factor of 2.001 was observed for BiOCl-OV and Au-BiOCl-OV.[27] In comparison with the Bi 4f XPS spectrum of Au-BiOCl (Figure S3b), two additional peaks of lower binding energies at 163.3 and 157.6 eV appear on that of Au-BiOCl-OV (Figure S3c). The decreased binding energies of Bi are originated from the partial reduction of Bi^{3+} by electrons localized at OVs.[27] Both OVs and Au NPs can largely modify the optical properties of oxide materials. Defect-free BiOCl exhibits an absorption edge at 370 nm in the UV region (Figure 1e). In contrast, BiOCl-OV shows an exponentially decaying tail across the visible region, corresponding to the absorption of OVs, and Au-BiOCl displays a broad LSPR band at 540 nm. The LSPR peak of colloidal Au NPs with diameters in the range of 30−35 nm in aqueous solutions is typically at 525 nm (Figure S5). The red plasmon shift is caused by an increase in the refractive index due to the BiOCl support. Au-BiOCl-OV combines the absorption characteristics of both BiOCl-OV and Au-BiOCl, as reflected by the existence of a long absorption tail and a broad LSPR peak (Figure 1e). The absorption of Au-BiOCl-OV spectrally matches well with the maximal emission of the simulated solar light from 450 to 650 nm, therefore ensuring the high light utilization efficiency (Figure 1f).

Hot Carrier Dynamics. SPV spectroscopy is a contactless and nondestructive technique for recording surface voltage changes.[28,29] It provides a direct and rapid probe of the photophysics within a photoresponsive material (Figure 2a, inset). No steady-state SPV signal was detected for defect-free BiOCl under visible light. In stark contrast with their absorption of visible light, neither Au NPs alone (Figure S6a and b) nor Au-BiOCl exhibit SPV responses (Figure 2a). When Au and n-type BiOCl are in contact, their Fermi levels will be aligned (Figure S7), along with the upward bending of the CB and VB of BiOCl toward the interface to form a Schottky barrier.[15,30] The silent SPV response of Au-BiOCl indicates that the Schottky barrier in this system is too high to allow for direct injection of hot electrons to the CB of BiOCl. Oxygen-deficient BiOCl-OV exhibits a distinct SPV response. The SPV response decays with the increase in the excitation light wavelength, which corresponds to the excitation of OVs (Figure 2a). Au deposition remarkably enhances the SPV response of BiOCl-OV. The good resemblance of the SPV response of Au-BiOCl-OV with its LSPR absorption spectrum clearly indicates the transfer of plasmonic hot electrons to BiOCl after the introduction of OVs (Figure 2a). The direct injection of hot electrons to oxygen-deficient BiOCl was also confirmed by photocurrent measurements in an electrochemical reaction cell under monochromatic light (Figures S6c,d and S8). Moreover,

the longer decay lifetime (0.19 ms) of the transient SPV of Au-BiOCl-OV in comparison with that (0.13 ms) of BiOCl-OV (Figure 2b) reveals that the lifetime of plasmonic hot electrons is longer than that of localized electrons on OVs.

The reason why OVs can facilitate the separation of plasmonic hot carriers can be explained by two possibilities. One is the lowering of the Schottky barrier, and the other is the introduction of new energy states to assist in extracting hot electrons. The former hypothesis is unlikely since OVs typically cause localized states, which hardly hybridize with the CB of BiOCl. The electrochemical Mott−Schottky plots of BiOCl and BiOCl-OV also reveal that the relative position of the CB of BiOCl indeed experiences no change after the introduction of OVs (Figure S9). Steady-state PL under the excitation of a 540 nm laser reveals that the OV-induced localized states are ∼0.42 eV below the CB edge of BiOCl according to the broad PL peak centered at 660 nm (Figure 2c). Therefore, OVs at a lower potential might offer a new channel for trapping plasmonic hot electrons, whose energies are not high enough to overcome the Schottky barrier. As a result, efficient separation of hot carriers is realized (Figure S10a,b).

Au deposition also remarkably enhances the PL emission intensity by ∼1.5 times (Figure 2c). The local electric field enhancement in the near-field regions around the Au NPs is believed to be responsible for the PL enhancement.[31−35] Such a PL enhancement vanishes under 420 nm excitation, where the LSPR of the Au NPs cannot be excited. This observation points out the importance of the spectral overlap between the LSPR of the Au NPs and the light absorption of BiOCl-OV. Therefore, as shown in Figure S10c,d, the locally enhanced electric field of the Au NPs can accelerate the excitation of hot electrons trapped on the OV states.[32,33,36−38] To help to further understand this process, finite-difference time-domain (FDTD) simulations were performed to calculate the electric field intensity distributions on the Au/BiOCl hybrid system.[39] The refractive index of BiOCl was taken from a previous study.[40] The simulated extinction spectra of this hybrid structure display the LSPR peak at 527 nm for the in-plane polarized excitation and at 540 nm for the out-of-plane polarized excitation (Figure 2d). The simulated LSPR band is close to the experimental one. The slight difference in the two excitation polarizations is originated from the different dielectric environments experienced by the collective electron oscillations in the two directions. Under the out-of-plane polarization, the electric field intensity enhancement contour reveals a spatially confined "hot spot" at the Au/BiOCl interface (Figure 2e). The electric field intensity enhancement in this "hot" region reaches over 500. This region is therefore the place where the excitation of trapped electrons to the CB of BiOCl is largely boosted.[35,37,38,41] On the other hand, we also performed time-resolved PL measurements (Figure 2c, inset). The experimental decaying profile of BiOCl-OV was fitted using a double-exponential function, giving an average lifetime ($\tau_{\text{BiOCl-OV}}$) of 0.88 ns. In comparison, Au-BiOCl-OV shows a faster PL decay, for which a third exponential term was added for a better fit. The resultant average lifetime $\tau_{\text{Au-BiOCl-OV}}$ is 0.52 ns. The reduced value of $\tau_{\text{Au-BiOCl-OV}}$ indicates that the PL emission is also coupled with the plasmonic field.[33,34] Although the LSPR band is spectrally separated from the PL emission peak, the low-energy tail of the LSPR band extends above 600 nm.

Photocatalytic Benzyl Alcohol Oxidation. The results above show that the defect states of OVs can facilitate the

separation of plasmonic hot carriers through trapping hot electrons and that further separation is facilitated by the plasmon-induced "hot spot" at the Au/BiOCl interface (Figure 2f). Successful separation of plasmonic hot carriers serves as the prerequisite for the subsequent triggering of chemical reactions, which, together with hot holes of a mild oxidizing ability and OVs for enhancing O_2 adsorption, makes Au-BiOCl-OV a promising photocatalyst for selective alcohol oxidation. BO was selected as the model substrate. Under visible light, BiOCl cannot oxidize BO, while BiOCl-OV gives 31.8% conversion in O_2 atmosphere (Table 1, entries 1 and 2). Unattractively,

Table 1. Photocatalytic BO Oxidation[a]

entry	catalyst	light	time/h	conversion (mol %)	selectivity (mol %)
1	BiOCl	visible	8		
2	BiOCl-OV	visible	8	31.8	80.3
3	Au-BiOCl	visible	8	7.3	93.9
4	Au-BiOCl-OV	visible	8	75.6	>99
5	Au-BiOCl-OV	UV	6	83.9	63.5

[a]The reactions were carried out in CH_3CN solutions (10 mL) containing the alcohol (0.5 mmol) and the catalyst (50 mg) in 0.1 MPa O_2 under a 300-W Xe lamp with a 420 nm cutoff filter or a 10-W UV light (λ = 365 nm).

besides BD, benzoic acid emerges as a byproduct, with a selectivity of 80.3% for BD. In Ar, conversion of BO over BiOCl-OV decreases dramatically to 2.8%, indicating that O_2 is the primary oxidant (Figure S11a). Au-BiOCl exhibits a higher selectivity (93.9%) for BO oxidation, but the conversion (7.3%) is very low (Table 1, entry 3). In contrast, remarkably, Au-BiOCl-OV shows the highest conversion of 75.6% with a selectivity exceeding 99% (Table 1, entry 4). We note that small Au NPs alone, with diameters below ∼10 nm, can be active toward direct BO oxidation in alkaline conditions even in dark.[42−45] However, in our study, the catalytic activities of the separately synthesized Au NPs in dark and under visible light irradiation, as well as those on BiOCl-OV in dark, are ruled out due to their relatively large size at 30−35 nm and the neutral reaction medium (Table S1). We also examined the catalytic activity of the mixture between BiOCl-OV and the Au NPs of 30−35 nm in size. The atomic ratio between the Au NPs and BiOCl-OV were adjusted to be the same as that for Au-BiOCl-OV. A conversion of 35.1% was obtained (Table S1). It is much smaller than that of Au-BiOCl-OV at 75.6% under the same conditions. In addition, the effect of the light power on the BO conversion was investigated by use of a green LED source, whose emission peak at λ = 530 nm was located within the LSPR band of Au-BiOCl-OV (Figure S12a). A high dependence of the photocatalytic BO oxidation activity on the light intensity was observed (Figure S12b), since a higher light power can provide more energy to the Au NPs. Taken together, these results further demonstrate that the photocatalytic activity of Au-BiOCl-OV is originated from the intimate interfacial charge transfer instead of the Au NPs. Conversion over Au-BiOCl-OV containing Au at different amounts shows a reversed U-shape, with an optimized atomic ratio of Au/BiOCl being 1.6% (Figure 3a). At a fixed Au loading amount of 1.6%, the concentration of OVs was shown to positively promote the photocatalytic BO oxidation conversion (Figure S13). Further increase in the Au loading amount causes the formation of larger Au NPs (Figure S14). Even though the increased amount
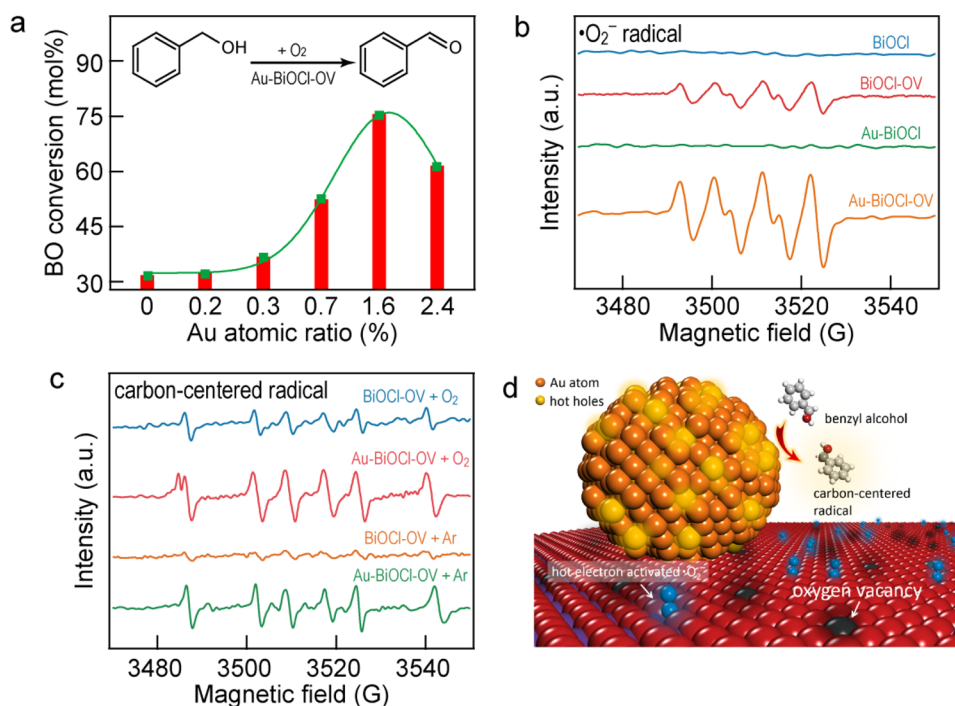
Figure 3. Photocatalytic BO oxidation and EPR detection. (a) Photocatalytic activities of Au-BiOCl-OV with different Au loading amounts. The atomic ratios of Au relative to BiOCl were determined by ICP-AES. (b, c) EPR detection of in situ formed $\bullet O_2^-$ and carbon-centered radicals, respectively, under different reaction conditions. The four-line and six-line spectra are the characteristic signals of DMPO-$\bullet O_2^-$ and DMPO-carbon-centered-radical adducts, respectively. (d) Schematic illustration of the generation of reactive species over Au-BiOCl-OV.

and size of Au NPs can lead to a more intense LSPR near-field and a higher optical absorption in BiOCl for more efficient photocatalysis,[46−49] larger Au NPs might occupy the OVs, therefore hindering the adsorption of O_2 on the BiOCl surface. As a result, the relationship between the Au loading amount and the photocatalytic activity can be a compromise among the number of reactive plasmonic charge carriers, the optical absorption, the Au NP size, and the accessibility of the OVs. Moreover, Au-BiOCl-OV can also photocatalyze a broad range of alcohols with high selectivities (Table S2).

In order to trace the origin of the high selectivity during BO oxidation over Au-BiOCl-OV, a series of control experiments on the trapping of active species were carried out. When $AgNO_3$ was added to trap electrons, conversion of BO over BiOCl-OV and Au-BiOCl-OV decreased significantly (Figure S11a). Since O_2 alone cannot oxidize BO, O_2 activation by electrons on OVs is therefore vital for BO oxidation. The activated O_2 responsible for BO oxidation was found to be superoxide radicals ($\bullet O_2^-$), as the addition of benzoquinone largely suppressed the BO oxidation over BiOCl-OV and Au-BiOCl-OV (Figure S11a). Transfer of hot electrons trapped on OVs to adsorbed O_2 is more efficient over Au-BiOCl-OV since both EPR and quantitative $\bullet O_2^-$ measurements showed that Au-BiOCl-OV possesses a higher $\bullet O_2^-$ generation capability than BiOCl-OV (Figure 3b and Figure S11b). The generated $\bullet O_2^-$ can be instantly consumed after the addition of BO (Figure S11b). Intriguingly, addition of sodium sulfide as a hole trapping reagent largely suppressed the BO conversion over Au-BiOCl-OV, while hardly affected that over BiOCl-OV. This suggests that BiOCl-OV photo-oxidizes BO with a high dependence on $\bullet O_2^-$, while hot holes and $\bullet O_2^-$ contribute together for this process over Au-BiOCl-OV. Unexpectedly, six new EPR peaks over BiOCl-OV and Au-BiOCl-OV emerged after the addition of BO. They can be assigned to carbon-

centered radicals (Figure 3c). Carbon-centered radicals are often considered as the key intermediates for photocatalytic BO oxidation, which can be induced either by reactive oxygen species or holes. When butylated hydroxytoluene was added to trap carbon-centered radicals, BO conversion over BiOCl-OV and Au-BiOCl-OV was indeed largely suppressed (Figure S11a). Plasmonic hot holes were found to oxidize BO to generate carbon-centered radicals with a higher priority than $\bullet O_2^-$, because when O_2 atmosphere was replaced with Ar, the EPR peaks were almost quenched for BiOCl-OV, but only slightly suppressed for Au-BiOCl-OV (Figure 3c). We therefore conclude that $\bullet O_2^-$ alone cannot selectively oxidize BO, while only when plasmonic holes of a mild oxidizing ability (to induce the formation of carbon-centered radicals) and hot electrons for O_2 activation (to induce the formation of $\bullet O_2^-$) are both present, can a high selectivity be achieved. There apparently exists a synergistic effect between plasmonic hot electrons and holes (Figure 3d). This synergistic effect was further supported by two control experiments. First, conversion of BO over Au-BiOCl-OV was largely decreased in Ar atmosphere, where hot electrons cannot activate O_2 to produce $\bullet O_2^-$ (Figure S11a). Second, under UV light, when BiOCl rather than the Au NPs was excited, Au-BiOCl-OV achieved a much higher conversion (83.9%) at a shorter reaction time, but the selectivity (63.5%) was low (Table 1, entry 5). About 30.5% of reacted BO was mineralized to CO_2 by strongly oxidizing holes on the VB of BiOCl according to the total organic carbon measurement.

Mechanistic Insights into BO Oxidation. In order to understand the high selectivity arising from the synergistic effect of plasmonic hot electrons and holes, we performed an isotopic labeling study using $^{18}O_2$ as the oxidant. No ^{18}O-labeled BD (BD_{O18}) was detected over BiOCl-OV, while 66% of BD was ^{18}O-labeled over Au-BiOCl-OV (Figure 4a). The
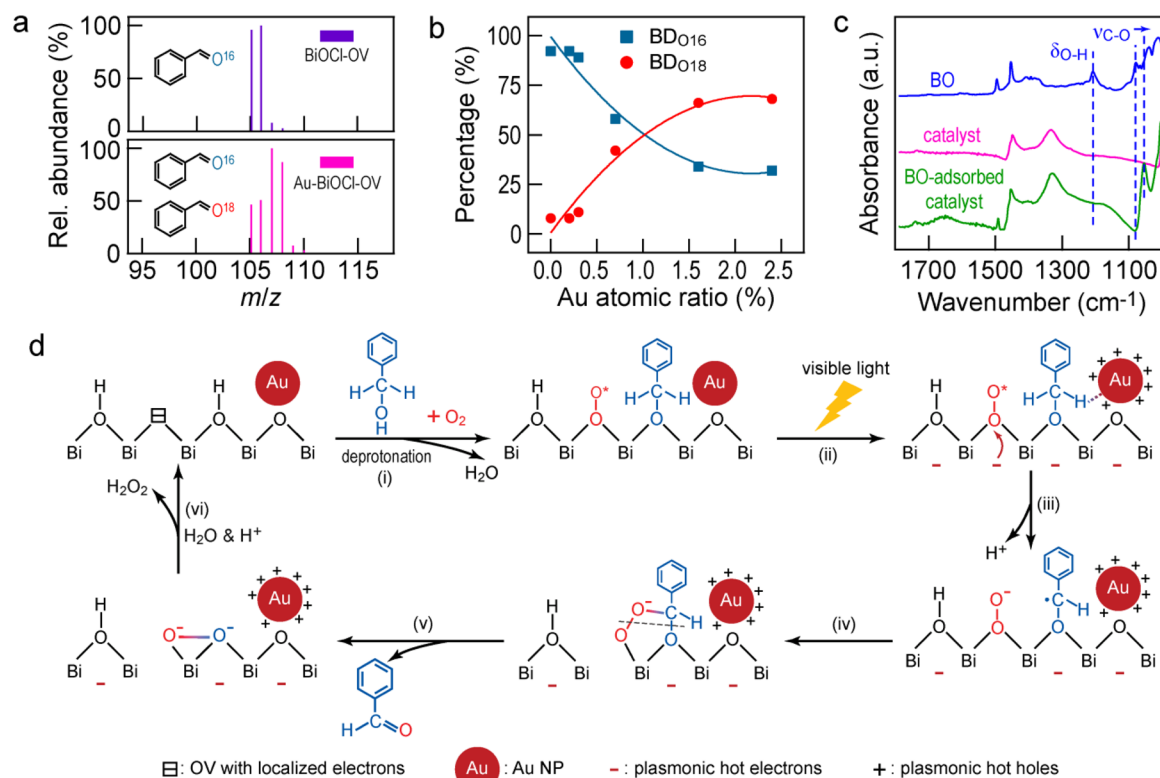
Figure 4. BO oxidation mechanism. (a) Mass spectra of BD produced in $^{18}O_2$ atmosphere over BiOCl-OV and Au-BiOCl-OV. (b) Relative proportion of ^{18}O-labeled BD along with the increase in the loading amount of Au over Au-BiOCl-OV. (c) FTIR spectra of pure BO and the photocatalyst (BiOCl-OV or Au-BiOCl-OV) before and after BO adsorption. (d) Proposed mechanism of selective BO oxidation over Au-BiOCl-OV.

relative percentage of BD_{O18} was found to increase along with the loading amount of Au and saturate at 68% (Figure 4b). Clearly, the Au NPs on BiOCl-OV offer a new reaction pathway for BO oxidation due to the introduction of hot carriers. FTIR spectroscopy revealed that the characteristic O—H band disappears, while the C—O band is strengthened and shifted to a lower wavenumber when BO is adsorbed either on BiOCl-OV or Au-BiOCl-OV (Figure 4c). This observation suggests the formation of a surface complex by a —C—O—Bi— coordinate bond.[6,50] Because the {001} surface of BiOCl is rich with surface hydroxyl groups, adsorption of BO is supposed to proceed through a deprotonation process to give an alkoxide intermediate and surface-bound water (Figure S15a). To verify this point, we treated Au-BiOCl-OV with NaF to partially replace the surface hydroxyl groups with F atoms.[51,52] Such a treatment reduced the BO conversion efficiency from 75.6 to 23.1%. For BO oxidation over BiOCl-OV, the unique surface structure first enables the coadsorption of O_2 and BO on the surface (i and ii in Figure S15b). Visible light promotes the activation of O_2 to surface $\bullet O_2^-$ by a localized electron. Surface $\bullet O_2^-$ alone is not effective in directly reacting with BO, but can readily react with surface-bound water to form a free $\bullet OOH$ radical and surface-bound hydroxide (OH$^-$) (ii and iii in Figure S15b). $\bullet OOH$ is more selective than $\bullet OH$ in abstracting the α-H of BO to give a carbon-centered radical without mineralizing BO or generating any phenol derivatives, along with the formation of H_2O_2 (iv in Figure S15b).[53] The carbon-centered radical is believed to undergo a subsequent back electron transfer, allowing for the retrapping of a localized electron and the formation of BD as well as a neutral vacancy.[53–55] Adsorption of OH$^-$ on the

neutral vacancy finally completes the catalytic cycle (v in Figure S15b). Low selectivity of BO oxidation over BiOCl-OV can be explained by O_2 dissociation on OVs, which induces the formation of strongly oxidative surface O adatoms in organic solvents, causing overoxidation of BD to acid (Figure S16a).[56,57] O_2 dissociation can also quench OVs, as suggested by the result that BiOCl-OV only maintained 12% of its initial reactivity in the fifth run (Figure S16b).

For Au-BiOCl-OV, BO gets adsorbed on Au-BiOCl-OV surface through a similar deprotonation pathway (i in Figure 4d). Upon the excitation of the Au NPs, hot electrons are quickly trapped at OVs, while hot holes remain on the Au surface (ii in Figure 4d). Even though the hot electrons and holes are spatially separated, the unique structure of the {001} surface of BiOCl-OV, which allows for the coadsorption of O_2 and BO, ensures the capability of the hot electrons and holes for coupled BO oxidation (Figure S15c,d). This is because hot holes on Au NPs can readily abstract the α-H of BO to form a carbon-centered radical, while trapped hot electrons are efficiently transferred to neighboring adsorbed O_2 to give surface-bound $\bullet O_2^-$ (iii in Figure 4d). The carbon-centered radical and $\bullet O_2^-$, both of which are of the radical nature and close to each other, are believed to be prone to recombine toward the formation of an oxygen-bridged structure,[11,58,59] manifesting a synergistic action between plasmonic hot electrons and holes (iv in Figure 4d). Concerted bond cleavage of this unique structure, as characterized by the simultaneous cleavage of the C—O bond of the alcohol and the O—O bond of O_2, highly favors the formation of BD and a BiOCl-bound peroxide-bridge structure (v in Figure 4d). If $^{18}O_2$ is used as the oxidant, then an ^{18}O transfer, from the dioxygen molecule to

the α-carbon atom of the alcohol, will occur, accounting for the origin of 66% ^{18}O-labeled BD during the Au-BiOCl-OV-catalyzed photoreaction. The BiOCl-bound peroxide-bridge structure was verified by a newly formed peak at 531.9 eV, which corresponds to the surface peroxide groups on the O 1s XPS spectra (Figure S17). The peroxide-bridge structure can readily react with an abstracted proton or surface-bound H_2O to form H_2O_2 and refresh the catalyst surface (vi in Figure 4d). The H_2O_2 generation rate over Au-BiOCl-OV is much faster than that over BiOCl-OV, indicating a higher O_2 utilization efficiency (Figure S11c,d). In addition, Au-BiOCl-OV exhibits better stability. It maintained over 83% of its initial reactivity after five times of repeated uses (Figure S16b). The color of Au-BiOCl-OV experienced no significant change during the catalytic processes, while the greyish yellow color of BiOCl-OV turned into pale white after use due to O_2 dissociation (Figure S16c). The clear color range of BiOCl-OV is consistent with its remarkably quenched EPR signal (Figure S16d), suggesting the instability of the OVs. We believe that the intensified local electric field at the Au/BiOCl interface might promote the transfer of trapped hot electrons at the OVs to adsorbed O_2, therefore lowering the possibility of O_2 dissociation over the OVs.

CONCLUSIONS

We have realized selective BO oxidation under visible light by depositing Au NPs on an oxygen-deficient BiOCl support. OVs on BiOCl facilitate the trapping and transfer of plasmonic hot electrons to adsorbed O_2, producing $\bullet O_2^-$ radicals, while hot holes remaining on the Au surface mildly oxidize BO to yield carbon-centered radicals. The proposed synergistic ring addition of these two radical species on the BiOCl surface highly favors the production of benzaldehyde along with an unexpected oxygen-atom transfer from O_2 to product. The knowledge acquired in this study, based on the full utilization of hot carriers generated within plasmonic metals on a rationally designed support, will contribute to the development of more active plasmonic catalysts for a wide range of organic transformations.

ASSOCIATED CONTENT

Ⓢ Supporting Information

The Supporting Information is available free of charge on the ACS Publications website at DOI: 10.1021/jacs.6b12850.

> Morphology, SEM images, XRD patterns, size distributions, XPS results, TEM characterization, photocurrent measurements, and Mott-Schottky plots (Figures S1–S17); and photocatalytic oxidations (Tables S1 and S2) (PDF)

AUTHOR INFORMATION

Corresponding Authors
*jfwang@phy.cuhk.edu.hk
*zhanglz@mail.ccnu.edu.cn

ORCID Ⓞ
Jianfang Wang: 0000-0002-2467-8751
Lizhi Zhang: 0000-0002-6842-9167

Notes
The authors declare no competing financial interest.

ACKNOWLEDGMENTS

REFERENCES

(1) Mallat, T.; Baiker, A. *Chem. Rev.* **2004**, *104*, 3037.
(2) Enache, D. I.; Edwards, J. K.; Landon, P.; Solsona-Espriu, B.; Carley, A. F.; Herzing, A. A.; Watanabe, M.; Kiely, C. J.; Knight, D. W.; Hutchings, G. J. *Science* **2006**, *311* (5759), 362−365.
(3) Mueller, J. A.; Goller, C. P.; Sigman, M. S. *J. Am. Chem. Soc.* **2004**, *126*, 9724.
(4) Abad, A.; Concepción, P.; Corma, A.; García, H. A. *Angew. Chem., Int. Ed.* **2005**, *44*, 4066.
(5) Su, F. Z.; Mathew, S. C.; Lipner, G.; Fu, X. Z.; Antonietti, M.; Blechert, S.; Wang, X. C. *J. Am. Chem. Soc.* **2010**, *132*, 16299.
(6) Liang, S. J.; Wen, L. R.; Lin, S.; Bi, J. H.; Feng, P. Y.; Fu, X. Z.; Wu, L. *Angew. Chem., Int. Ed.* **2014**, *53*, 2951.
(7) Lang, X. J.; Ma, W. H.; Chen, C. C.; Ji, H. W.; Zhao, J. C. *Acc. Chem. Res.* **2014**, *47*, 355.
(8) Yurdakal, S.; Palmisano, G.; Loddo, V.; Augugliaro, V.; Palmisano, L. *J. Am. Chem. Soc.* **2008**, *130*, 1568.
(9) Pichat, P.; Mozzanega, M.-N.; Courbon, H. *J. Chem. Soc., Faraday Trans. 1* **1987**, *83*, 697.
(10) Zhang, M.; Chen, C. C.; Ma, W. H.; Zhao, J. C. *Angew. Chem., Int. Ed.* **2008**, *47*, 9730.
(11) Navio, J. A.; Gómez, M. G.; Pradera Adrian, M. A.; Mota, J. F. *J. Mol. Catal. A: Chem.* **1996**, *104*, 329.
(12) Tsunoyama, H.; Ichikuni, N.; Sakurai, H.; Tsukuda, T. *J. Am. Chem. Soc.* **2009**, *131*, 7086.
(13) Zhang, B.; Li, J.; Zhang, B. Q.; Chong, R. F.; Li, R. G.; Yuan, B.; Lu, S.-M.; Li, C. *J. Catal.* **2015**, *332*, 95.
(14) Choi, W. *Catal. Surv. Asia* **2006**, *10*, 16.
(15) Li, B. X.; Gu, T.; Ming, T.; Wang, J. X.; Wang, P.; Wang, J. F.; Yu, J. C. *ACS Nano* **2014**, *8*, 8152.
(16) Tsukamoto, D.; Shiraishi, Y.; Sugano, Y.; Ichikawa, S.; Tanaka, S.; Hirai, T. *J. Am. Chem. Soc.* **2012**, *134*, 6309.
(17) Tanaka, A.; Hashimoto, K.; Kominami, H. *J. Am. Chem. Soc.* **2012**, *134*, 14526.
(18) Naya, S.; Inoue, A.; Tada, H. *J. Am. Chem. Soc.* **2010**, *132*, 6292.
(19) Kimura, K.; Naya, S.; Jin-nouchi, Y.; Tada, H. *J. Phys. Chem. C* **2012**, *116*, 7111.
(20) Naya, S.; Teranishi, M.; Isobe, T.; Tada, H. *Chem. Commun.* **2010**, *46*, 815.
(21) Brongersma, M. L.; Halas, N. J.; Nordlander, P. *Nat. Nanotechnol.* **2015**, *10*, 25.
(22) Mubeen, S.; Hernandez-Sosa, G.; Moses, D.; Lee, J.; Moskovits, M. *Nano Lett.* **2011**, *11*, 5548.
(23) Mubeen, S.; Lee, J.; Singh, N.; Krämer, S.; Stucky, G. D.; Moskovits, M. *Nat. Nanotechnol.* **2013**, *8*, 247.
(24) Jiang, J.; Zhao, K.; Xiao, X. Y.; Zhang, L. Z. *J. Am. Chem. Soc.* **2012**, *134*, 4473.
(25) Zhao, K.; Zhang, L. Z.; Wang, J. J.; Li, Q. X.; He, W. W.; Yin, J. J. *J. Am. Chem. Soc.* **2013**, *135*, 15750.
(26) Li, H.; Shang, J.; Ai, Z. H.; Zhang, L. Z. *J. Am. Chem. Soc.* **2015**, *137*, 6393.
(27) Li, H.; Shi, J. G.; Zhao, K.; Zhang, L. Z. *Nanoscale* **2014**, *6*, 14168.
(28) Kronik, L.; Shapira, Y. *Surf. Sci. Rep.* **1999**, *37* (1-5), 1−206.
(29) Kronik, L.; Shapira, Y. *Surf. Interface Anal.* **2001**, *31*, 954−965.
(30) Liu, G. G.; Wang, T.; Zhou, W.; Meng, X. G.; Zhang, H. B.; Liu, H. M.; Kako, T.; Ye, J. H. *J. Mater. Chem. C* **2015**, *3*, 7538.
(31) Ming, T.; Chen, H. J.; Jiang, R. B.; Li, Q.; Wang, J. F. *J. Phys. Chem. Lett.* **2012**, *3*, 191.

(32) Atwater, H. A.; Polman, A. *Nat. Mater.* **2010**, *9*, 205.

(33) Wu, J.-L.; Chen, F.-C.; Hsiao, Y.-S.; Chien, F.-C.; Chen, P. L.; Kuo, C.-H.; Huang, M. H.; Hsu, C.-S. *ACS Nano* **2011**, *5*, 959.

(34) Munechika, K.; Chen, Y.; Tillack, A. F.; Kulkarni, A. P.; Plante, I. J.-L.; Munro, A. M.; Ginger, D. S. *Nano Lett.* **2011**, *11*, 2725.

(35) Awazu, K.; Fujimaki, M.; Rockstuhl, C.; Tominaga, J.; Murakami, H.; Ohki, Y.; Yoshida, N.; Watanabe, T. *J. Am. Chem. Soc.* **2008**, *130*, 1676.

(36) Thimsen, E.; Le Formal, F.; Grätzel, M.; Warren, S. C. *Nano Lett.* **2011**, *11*, 35.

(37) Gao, H. W.; Liu, C.; Jeong, H. E.; Yang, P. D. *ACS Nano* **2012**, *6*, 234.

(38) Liu, Z. W.; Hou, W. B.; Pavaskar, P.; Aykol, M.; Cronin, S. B. *Nano Lett.* **2011**, *11*, 1111.

(39) Gallinet, B.; Butet, J.; Martin, O. J. F. *Laser Photonics Rev.* **2015**, *9*, 577.

(40) Bannister, F. A.; Hey, M. H. *Mineral. Mag.* **1935**, *24*, 49.

(41) Ingram, D. B.; Linic, S. *J. Am. Chem. Soc.* **2011**, *133*, 5202.

(42) Zope, B. N.; Hibbitts, D. D.; Neurock, M.; Davis, R. J. *Science* **2010**, *330*, 74.

(43) Tsunoyama, H.; Sakurai, H.; Negishi, Y.; Tsukuda, T. *J. Am. Chem. Soc.* **2005**, *127*, 9374.

(44) Su, F.-Z.; Liu, Y.-M.; Wang, L.-C.; Cao, Y.; He, H.-Y.; Fan, K.-N. *Angew. Chem., Int. Ed.* **2008**, *47*, 334.

(45) Abad, A.; Corma, A.; García, H. *Chem. - Eur. J.* **2008**, *14*, 212.

(46) Seh, Z. W.; Liu, S. H.; Low, M.; Zhang, S.-Y.; Liu, Z. L.; Mlayah, A.; Han, M.-Y. *Adv. Mater.* **2012**, *24*, 2310.

(47) Qian, K.; Sweeny, B. C.; Johnston-Peck, A. C.; Niu, W. X.; Graham, J. O.; DuChene, J. S.; Qiu, J. J.; Wang, Y.-C.; Engelhard, M. H.; Su, D.; Stach, E. A.; Wei, W. D. *J. Am. Chem. Soc.* **2014**, *136*, 9842.

(48) Chen, H. J.; Shao, L.; Li, Q.; Wang, J. F. *Chem. Soc. Rev.* **2013**, *42*, 2679.

(49) Jiang, R. B.; Li, B. X.; Fang, C. H.; Wang, J. F. *Adv. Mater.* **2014**, *26*, 5274.

(50) Shishido, T.; Miyatake, T.; Teramura, K.; Hitomi, Y.; Yamashita, H.; Tanaka, T. *J. Phys. Chem. C* **2009**, *113*, 18713.

(51) Kim, H.; Choi, W. *Appl. Catal., B* **2007**, *69*, 127.

(52) Wang, Q.; Chen, C. C.; Zhao, D.; Ma, W. H.; Zhao, J. C. *Langmuir* **2008**, *24*, 7338.

(53) Hallett-Tapley, G. L.; Silvero, M. J.; González-Béjar, M.; Grenier, M.; Netto-Ferreira, J. C.; Scaiano, J. C. *J. Phys. Chem. C* **2011**, *115*, 10784.

(54) Li, R. H.; Kobayashi, H.; Guo, J. F.; Fan, F. *J. Phys. Chem. C* **2011**, *115*, 23408.

(55) Ohno, T.; Izumi, S.; Fujihara, K.; Masaki, Y.; Matsumura, M. *J. Phys. Chem. B* **2000**, *104*, 6801.

(56) Tripathy, J.; Lee, K.; Schmuki, P. *Angew. Chem., Int. Ed.* **2014**, *53*, 12605.

(57) Furukawa, S.; Shishido, T.; Teramura, K.; Tanaka, T. *ACS Catal.* **2012**, *2*, 175.

(58) Zhang, M.; Wang, Q.; Chen, C. C.; Zang, L.; Ma, W. H.; Zhao, J. C. *Angew. Chem., Int. Ed.* **2009**, *48*, 6081.

(59) Shiraishi, Y.; Kanazawa, S.; Tsukamoto, D.; Shiro, A.; Sugano, Y.; Hirai, T. *ACS Catal.* **2013**, *3*, 2222.